Heliyon

Stand-alone containment analysis of Phébus FPT tests with ASTEC and MELCOR codes: the FPT-2 test

Bruno Gonfiotti[*], **Sandro Paci**

University of Pisa, Dipartimento di Ingegneria Civile e Industriale (DICI), Largo Luciano Lazzarino 2, 56122, Pisa, Italy

[*] Corresponding author.

E-mail address: bruno.gonfiotti@for.unipi.it (B. Gonfiotti).

Abstract

During the last 40 years, many studies have been carried out to investigate the different phenomena occurring during a Severe Accident (SA) in a Nuclear Power Plant (NPP). Such efforts have been supported by the execution of different experimental campaigns, and the integral Phébus FP tests were probably some of the most important experiments in this field. In these tests, the degradation of a Pressurized Water Reactor (PWR) fuel bundle was investigated employing different control rod materials and burn-up levels in strongly or weakly oxidizing conditions. From the findings on these and previous tests, numerical codes such as ASTEC and MELCOR have been developed to analyze the evolution of a SA in real NPPs. After the termination of the Phébus FP campaign, these two codes have been furthermore improved to implement the more recent findings coming from different experimental campaigns. Therefore, continuous verification and validation is still necessary to check that the new improvements introduced in such codes allow also a better prediction of these Phébus tests. The aim of the present work is to re-analyze the Phébus FPT-2 test employing the updated ASTEC and MELCOR code versions. The analysis focuses on the stand-alone containment aspects of this test, and three different spatial nodalizations of the containment vessel (CV) have been developed. The

paper summarizes the main thermal-hydraulic results and presents different sensitivity analyses carried out on the aerosols and fission products (FP) behavior. When possible, a comparison among the results obtained during this work and by different authors in previous work is also performed. This paper is part of a series of publications covering the four Phébus FP tests using a PWR fuel bundle: FPT-0, FPT-1, FPT-2, and FPT-3, excluding the FPT-4 one, related to the study of the release of low-volatility FP and transuranic elements from a debris bed and a pool of melted fuel.

Keywords: Safety engineering, Nuclear engineering

1. Introduction

In the last 40 years, many studies have been carried out to investigate the FP release from a damaged nuclear core and their subsequent behavior in the primary circuit and the containment system of a NPP during a SA sequence [1, 2, 3]. Separate-effect tests as well as integral-effect tests have been performed in different experimental campaigns. Among all these experimental campaigns, only the international Phébus FP experimental program was devoted to the study of a SA in all its different phases and aspects [4]. This experimental campaign was conducted between 1998 and 2010 in the integral Phébus FP facility at the Cadarache Study Center (France). Five integral tests were performed, investigating the main processes affecting the severe degradation of the nuclear fuel and control rods, the release of FP and control materials, their transport through the reactor coolant circuit as well as their deposition as aerosols in the CV [5, 6, 7]. Different fuel burn-ups, control rod materials, and thermal-hydraulic conditions were investigated [8]. The Phébus FP research program has provided a comprehensive database to improve the understanding of the various phenomena characterizing the fission product behavior. Furthermore, these experiments are the most representative integral-effect tests ever performed, also forming a valuable validation database for several severe accident codes [9]. In detail, the FPT-2 test employed a moderately irradiated fuel bundle (overall burn-up of 31.8 GWd/t), with an Ag-In-Cd control rod, under steam-poor conditions inside the rod bundle [10]. In the present paper, a stand-alone containment analysis of this test is presented, employing recent releases of two of the most world-wide employed SA codes: ASTEC v2.0 revision 3 patch 3 and MELCOR v2.1.6840. Both these integral codes can simulate a SA from the initiating event until the release of FP outside the containment. The aim of the work is to investigate the main parameters influencing the FP behavior inside the CV during the four main phases of the test (degradation, aerosol, washing, and chemistry phases). Different previous analyses (for the full-plant or the stand-alone containment) have employed too complex or too coarse

nodalizations [11, 12, 13, 14, 15], not able to reproduce the main thermal-hydraulic or aerosol phenomena, or to be employed for full-plant analysis.

For this purpose, three different spatial nodalizations of the Phébus CV have been developed and investigated with the recent ASTEC V2.0 and MELCOR 2.1 versions. The simplest model consists of 6 volumes, 8 walls, and 7 junctions, while the most complex one consists of 21 volumes, 15 walls, and 32 junctions. These three nodalizations have been kept as simple as possible (as number of volumes and walls) to allow a similar spatial schematization also for future full plant analysis. These nodalizations have been also developed in the most identical way possible for both codes, but the different modelling approach of certain aspects were all exploited to show the capabilities of each code.

Moreover, most of the previous analyses have been performed employing older AS-TEC V1 and MELCOR V1.8.5 versions. Several differences exist between these older code versions and the newer ones employed in the present work: MELCOR was completely re-engineered and written in a more recent Fortran version, but the main modelling aspects remained quite the same [16]. In turn, several modelling improvements were introduced in ASTEC [17]: for the containment thermal-hydraulic section mainly numerical refinements and bugs fixing were implemented, while for the aerosol behavior and the FP chemistry in containment, the radiochemistry of ruthenium was introduced, the chemistry of iodine in the gas and the liquid phases was revised to reflect the actual state-of-the-art [18], and the dry aerosols re-suspension model was improved.

The present paper is a part of a series of publications, covering the 4 Phébus FP tests carried out using a PWR fuel bundle: FPT-0 [19], FPT-1 [20], FPT-2, and FPT-3. Observations made during these analyses led to a thorough understanding of the in-containment source term and its coupling with thermal hydraulics under unsaturated but condensing atmospheres.

2. Background

2.1. The Phébus FP facility

The Phébus FP facility is a downscaled reproduction (5000:1) of a typical French 900 MWe class Pressurized Water Reactor (PWR). A schematic sketch of the facility is shown in Fig. 1 [4]. The first component is the driver core and its cooling circuit, encapsulated inside a cylindrical shroud. The core consists of a PWR fuel bundle (test assembly), two instrumented fuel rods as driver, and a control rod. During the test, the driver core is heated-up and irradiated to recreate the temperature increase supposed to occur during a Loss Of Coolant Accident (LOCA) and the FP build-up during normal operation. Steam is injected at the bottom of the shroud to
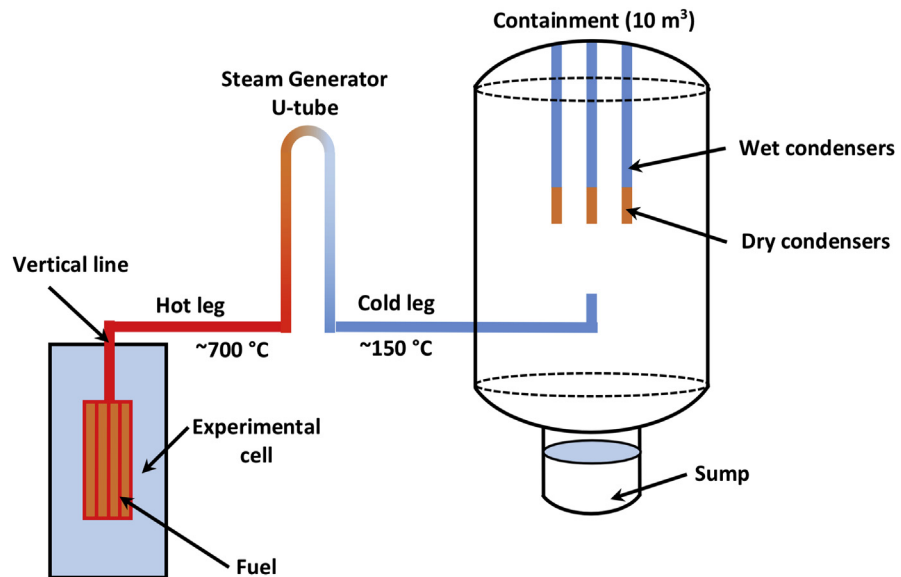
Fig. 1. Schematic Overview of the Phébus FP facility (image redrawn basing on that appearing in Ref. [4]).

reproduce the Steam-Zircaloy reaction occurring in a real core during a SA, and to ease the FP transport through the primary circuit and into the CV. The primary circuit consists of three parts: the hot leg, the U-tube SG, and the cold leg. The final part of the cold leg enters into the CV to reproduce conditions of a cold leg LOCA.

The CV has a total free volume of 10 m^3, a height of about 5 m, an inner diameter of about 1.8 m, and a cylindrical shape with a water sump in the lower part. The sump has a height of 0.6 m and an inner diameter of 0.584 m to reproduce a representative atmosphere-water exchange surface [21]. The CV walls are made of stainless steel (AISI 316L), and their temperatures are controlled through two independent systems to decouple the sump water temperature from the gas temperature, and to avoid condensation onto the cylindrical CV walls. A spray system fed only by the water contained in the sump is also inserted in the lower CV zone to wash-down the FP settled on the vessel bottom surfaces.

Three condensers (diameter 0.15 m each) are connected at the CV top vault to simulate the cold structures of a reactor building. The main aim of these condensers is to allow control of the heat transfer and steam condensation. Each condenser is divided into a "dry" part (0.782 m length) and a "wet" part (1.718 m length), and two independent cooling loops control the surface temperature of each part. The wet part is also covered with an epoxy paint, to allow organic iodine formation. Further details on the facility can be found in the final reports of each experiment [10, 22, 23, 24].

2.2. The FPT-2 test and its boundary conditions

The Phébus FPT-2 test can be subdivided into four different phases:

- The degradation phase from 0 s to 23,880 s (6.63 h), when the driver core is heated-up to allow the progressive melting of the test fuel rod and the subsequent release of FP towards the CV. The employed fuel consists in a PWR rod bundle with an overall burnup of 31.8 GWd/t and an Ag-In-Cd control rod. The core degradation occurs in a weakly oxidizing atmosphere.

- The aerosol phase from 24,240 s (6.73 h) to 157,140 s (43.65 h), with the CV maintained in stable conditions and isolated from the core (isolation occurs at 24,240 s−6.73 h).

- The washing phase from 157,140 s (43.65 h) to 177,060 s (49.18 h), with the activation of the spray inside the CV, to wash-down the FP settled onto the elliptic bottom and to collect them into the sump water.

- The chemistry phase from 177,060 s (49.18 h) to 375,780 s (104.38 h), with the CV in stable conditions to investigate the iodine chemistry in the sump water.

During the degradation phase, while the core is heated-up, a steam injection at the bottom of the driver core with an almost constant mass flow rate occurs (0.46 g/s). The heat provided leads to progressive damage of the nuclear fuel, and the steam injection supports the transport of FP and Structural Materials (SM) through the primary circuit and into the CV. Once in the CV, the steam condenses onto the wet parts of the three condensers, while the SM and the FP deposit onto the CV surfaces. Even H_2 enters into the CV due to the steam-Zircaloy reaction occurring in the fuel bundle. Small nitrogen and helium mass injections (few mg/s) also occur for the proper operation of two sensors placed along the primary circuit.

In the following aerosol phase, the CV is isolated from the primary circuit and kept in stable thermal-hydraulics conditions to allow the complete SM and FP settling. In this second phase, the small helium injection stops, while the nitrogen injection continues because the corresponding sensor is positioned after the valve that "isolate" the primary circuit from the CV itself.

Once reached the required conditions, the washing phase takes place. This phase is mainly characterized by the activation of a water spray loop, washing the bottom surfaces of the CV elliptic bottom. At the same time, the sump, and the dry and wet condenser temperatures were also decreased. The first one was decreased to reduce steam evaporation while the others two to enhance condensation onto these structures.

After the washing phase, the sump and the wet condenser temperatures were again increased. The sump up to 120 °C, while the wet condenser up to 95 °C. Then, the whole CV conditions were kept constant until the end of the test.

Since only the containment part of the test was analyzed, the mass flow rates from the primary circuit were considered as boundary conditions, as well as the outer CV wall temperatures. A more detailed description of the test can be found in the FPT-2 Final Report [10].

2.3. Employed codes

As previously said, two codes have been employed for the analysis presented in the paper: ASTEC v.2.0 revision 3 patch 3 and MELCOR V2.1.6840. Both codes are capable to simulate a SA from the initiating event to the release of FP outside the containment. Both ASTEC and MELCOR are lumped-parameter codes, with the spatial domain subdivided into volumes connected by means of junctions. Volumes are usually in non-equilibrium conditions (atmosphere and pool — if any — with different temperatures), and a simplified momentum balance equation reproduces the transport of fluids across the junctions. Both codes include also additional packages/modules to couple thermal-hydraulics with aerosol/FP calculations. Significant differences exist regarding the aerosol and FP treatment in terms of models, numerical approach, and coupling with thermal-hydraulics, but such differences will not be discussed in the present paper.

ASTEC V2.0 - developed by the Institut de Radioprotection et de Sûreté Nucléaire (IRSN) and the Gesellschaft für Anlagen und Reaktorsicherheit mbH (GRS) - is composed of several modules, but only CPA, IODE and SYSINT were employed in the present work. CPA deals with the containment thermal-hydraulics and aerosol behavior [25], IODE with the Iodine and Ruthenium chemistry in containment [26], and SYSINT manages safety systems based on user-inputs or plant conditions [27].

MELCOR - developed by Sandia National Laboratory (USA) under the sponsorship of the US Nuclear Regulatory Commission (USNRC) - is composed of several packages. Most of these packages were employed in the present work, the main ones being the Control Volume Hydrodynamic (CVH), the FLow path (FL), the Heat Structure (HS), and the containment SPRay (SPR) for the thermal-hydraulic analysis, and the RadioNuclide (RN) package for the analysis of aerosol behavior [16, 28].

3. Model

Three spatial nodalizations have been developed to simulate the CV behavior in the FPT-2 test (Fig. 2) [10]. All the initial conditions have been set according to data reported in the FPT-2 Final Report [10].

The first scheme (M1) consists of 6 volumes plus one to simulate the outer environment, 7 junctions, and 8 walls. The main cylindrical part of the CV is subdivided into two radial rings, and the sump has an initial water inventory of 110 kg. The
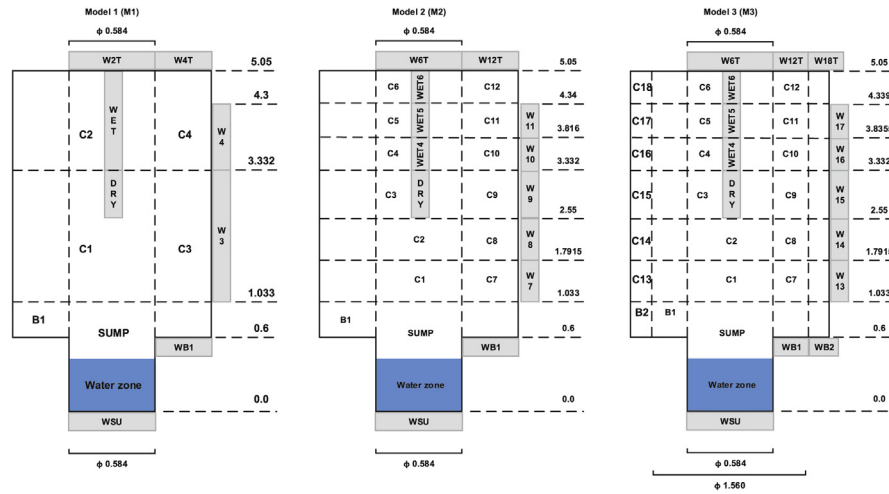
Fig. 2. Sketch of the employed nodalizations — Model 1 (M1) on the left, Model 2 (M2) in the middle, and Model 3 (M3) on the right.

atmosphere is filled with a mixture of 5% O_2 and 95% N_2 in the MELCOR runs (as reported in the FPT-2 Final Report [10]), and with normal air in the ASTEC ones. This difference has no influence on the obtained results as stressed in the sensitivity analyses section. The different volumes are connected by means of junctions, and 8 walls are added to simulate the sump outer wall (WSU), the semi-elliptic bottom and CV top parts (WB1, W2T, and W4T), the cylindrical outer wall (W3, W4), and the three condensers (WET and DRY). Except WET and DRY, all these walls were simulated with an imposed outer temperature evolving in time [10], and with an inner temperature based on heat exchange with their surrounding volumes. The Characteristic Lengths (CLs) of such walls were calculated according to Eq. (1):

$$\begin{cases} Vertical\ cylinders \rightarrow CL = Height\ of\ the\ wall \\ Horizontal\ surfaces \rightarrow CL = Area\ of\ the\ wall/Perimeter\ of\ the\ wall \end{cases} \tag{1}$$

The first correlation is taken from the CPA theory manual [25] and from a Sandia report on the nodalization of PWR containments [29], while the second one is taken from [29].

On the other hand, the WET and DRY walls were simulated with an inner temperature evolving in time [10] and with an outer temperature basing on the conditions of their surrounding volumes. The characteristic lengths of DRY and WET HSs were set equal to their external diameter (0.15 m) because such dimension was found capable to predict a condensation rate closer to the experimental one. The discrepancy between the strategies to evaluate the CL is due to the film condensation models implemented in ASTEC and MELCOR that are not suitable to describe the dropwise condensation probably occurring on the condenser surfaces. For the ASTEC code similar problems and explanations were also found [11], and in this paper

CL values of about 0.01−0.02 m were suggested. Although, in the present analysis values of the same order of magnitude provided too high condensation rates. The solutions proposed in [11] and in this paper stress that the CL of inner walls is still an open question, and so a possible source of user's effect in the calculation results.

Additional junctions and walls were also introduced in the ASTEC and MELCOR input decks to support the thermal-hydraulics and aerosol calculations. Additional walls were introduced on the bottom of the volumes simulating the CV main cylindrical part to provide a settling area for FP deposition as suggested in [16]. Three additional junctions were added to the ASTEC input deck to simulate the water draining from the wet condensers into the sump and the sprays injection. Instead, to simulate the water draining from the wet condensers to the water sump, two walls were added in the MELCOR input deck. These different approaches followed to simulate the water draining are due to the different models implemented in the codes.

In turn, spray injection is simulated through junctions in both the MELCOR and AS-TEC codes. Filter presence was also added at the inlet of these junctions to avoid the transport of FP. Main data of this spray injection are reported in Table 1.

Injections and samplings were assumed to occur in the control volume directly above the SUMP one, and their time trends were set according to the data reported in the FPT-2 Final Report [10]. The Aerodynamic Mass Median Diameter (AMMD) and the Geometric Standard Deviation (GSD) of the different FP and aerosol injections are reported in Table 2. These time dependent values were employed only in AS-TEC, because MELCOR accepts only constant values. For this reason, in MELCOR, the Iodine injection was simulated with an AMMD of 2.85 μm and a GSD of 2.9, and the other FP injections with an AMMD of 2.67 μm and a GSD of 2.

The second spatial scheme (M2) is a more refined one, and it consists of 14 volumes plus one for the outer environment, 19 junctions, and 13 walls. The spatial subdivision of the CV is more refined, but the vessel cylindrical zone is still subdivided only into two radial rings. As for the previous M1 scheme, additional walls and junctions have been introduced to simulate the spray injection, the draining of the condensed water onto wet condenser surfaces, and to support the aerosol and FP calculations. For ASTEC five additional junctions are schematized: three to simulate the draining of water from the wet condenser surfaces (WET4, WET5, and WET6) into the sump, and the other two to simulate the spray injection. In the MELCOR input deck the

Table 1. Spray characteristics.

Activation time	175,680 s (48.8 h)
Deactivation time	177,060 s (49.18 h)
Droplet diameter	$12 \cdot 10^{-4}$ m
Mass Flow rate	$1.417 \cdot 10^{-3}$ m^3/s

Table 2. AMMD and GSD of the different FP and aerosol injections.

Time [s]	Time [h]	Elements				
		W, Pm, La, Y, Ce, Te, Mo, Tc, Sn, Re, Rb, Sr, Zr, Cs, Ba, Ru, Ag, Cd, In, U		**I**		
		AMMD [μm]	**GSD [−]**	**AMMD [μm]**	**GSD [−]**	
9,000	2.5	1.4	2.08	1.41	2.09	
10,424	2.9	1.4	2.08	1.41	2.09	
10,632	2.95	1.4	2.08	1.41	2.09	
15,597	4.33	2.5	1.89	2.62	1.85	
15,802	4.39	2.5	1.89	2.62	1.85	
20,790	5.78	3.73	1.94	4.08	1.97	
20,889	5.8	3.73	1.94	4.08	1.97	
23,765	6.6	3.68	2.32	4.07	2.34	
24,070	6.69	3.68	2.32	4.07	2.34	

water draining from the upper wall (WET6) to the lower walls (WET5 and WET4) is correctly simulated, but the direct transport of the water from the upper zone (C4) into the sump is still simulated as in M1 model. All the other assumptions made for M1 are also valid for M2.

The third spatial scheme (M3) has the CV main cylindrical zone subdivided into three radial rings, and it consists in 21 volumes plus one for the outer environment, 32 junctions, and 15 walls. As for the previous schemes, fictitious junctions and walls are added to simulate the spray injection, the draining of the condensed water onto wet condenser surfaces into the sump, and to support the aerosol and FP calculations.

4. Results & discussion

4.1. Thermal-hydraulic results

The correctness of the thermal-hydraulic predictions is of major importance, because of its influence on the overall aerosol and FP behavior, especially on the iodine chemistry.

The total pressure evolutions predicted by the two codes inside the CV are shown in Figs. 3, 4, and 5, together with the experimental data. Until 40,000 s (11.1 h - Fig. 3) no appreciable discrepancies among experimental data and code predictions are shown. After this time, differences start to appear: a slow decrease of the total pressure is shown in the experiment, but the two codes fail to catch this trend reproducing an almost constant pressure evolution. During this phase, the total pressure evolution
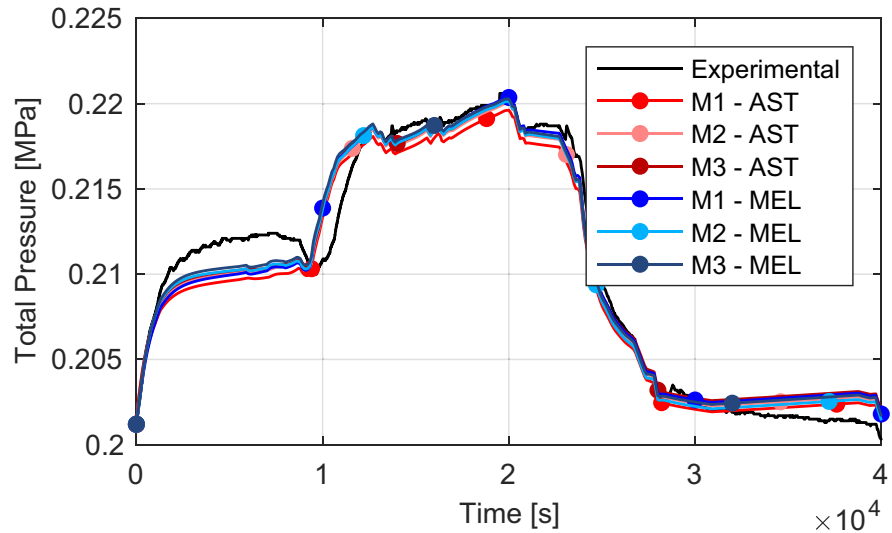
Fig. 3. Total pressure evolution during the degradation and the early aerosol phases.

is guided by continuous N_2 and He injections - needed for the proper operation of two sensors placed along the primary circuit - and by the steam condensation. In the experiment, the positive contribution given by N_2 and He injections seems not able to counteract the negative contribution coming from the steam condensation, thus a slow pressure decrease occurs. Both codes are capable to reproduce the positive effect of N_2 and H_2 injections, but fail on the steam partial pressure evolution. This explanation is supported by the experimental relative humidity (r.h.) trend shown during this phase (Fig. 6): in the experiment a slow decrease from 55% to
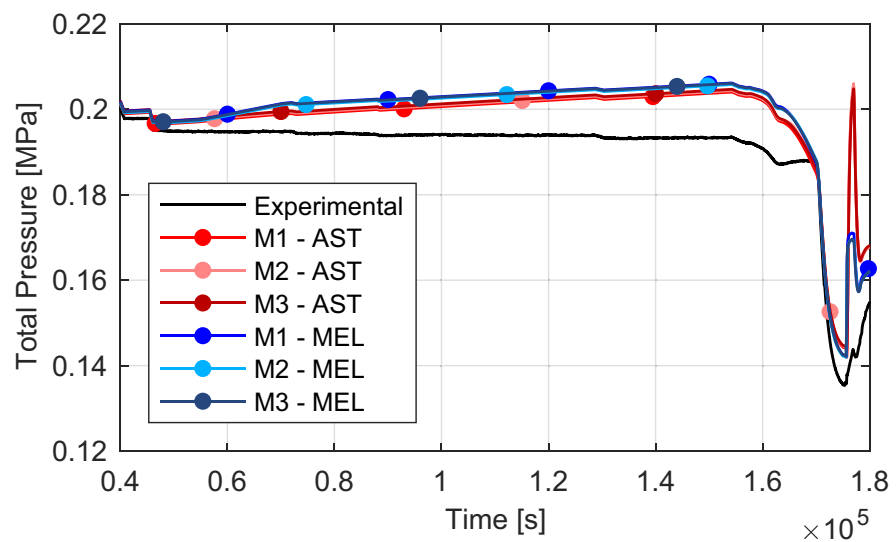
Fig. 4. Total pressure evolution during the aerosol and the early washing phases.
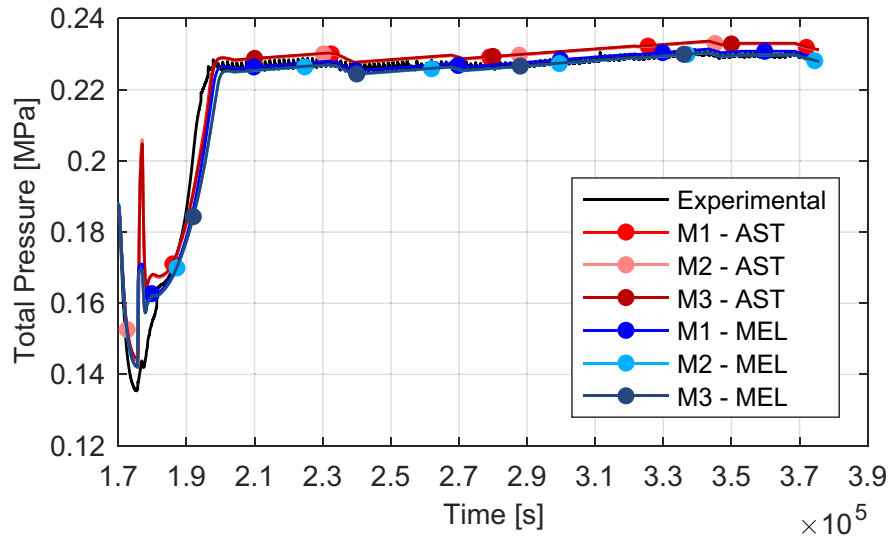
Fig. 5. Total pressure evolution during the washing and the chemistry phases.

47% is shown, while constant values are shown in the ASTEC (52%) and MELCOR (55%) calculations.

Two actions were performed during the test between 162,000 s (45 h) and 170,000 s (47.22 h): the reduction of the sump water temperature from 90 °C to 42 °C, and the reduction (from 110 °C to 90 °C) and the subsequent re-increase (120 °C) of the vessel wall temperature. During this time window both codes fail to catch the experimental total pressure trend, because of incorrect estimation of the influence of these two actions.
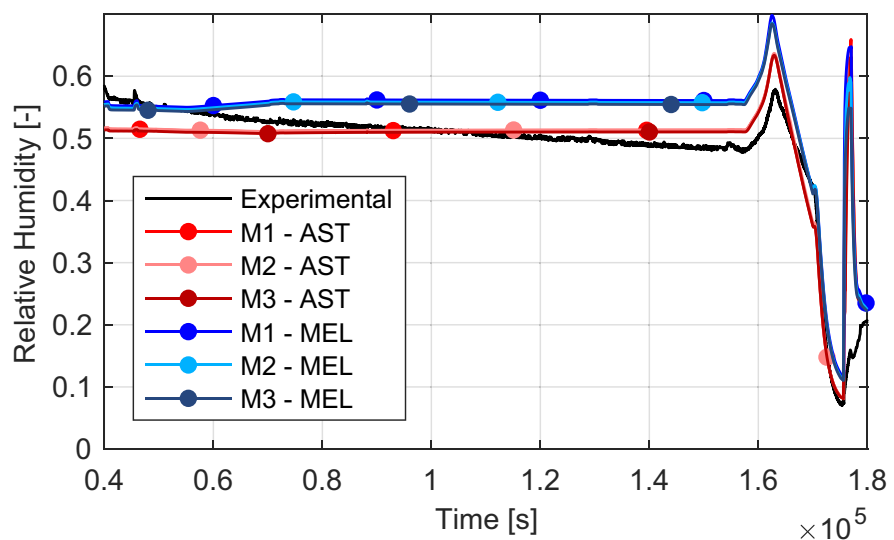
Fig. 6. Relative humidity evolution during the aerosol and the early washing phases.

During the following washing and chemistry phases the predictions are quite good (Fig. 5), except during the sprays operation (175,680 s−177,060 s i.e. 48.8 h−49.18 h). During this time window, in the experiment the pressure slowly increases, while a spike is shown by both codes. These differences last up to 182,000 s (50.56 h), then the predictions became again comparable with the experimental data.

The atmospheric temperature evolutions during the degradation phase at 2.32 m, 3.0 m, and 4.02 m elevations inside the CV are shown in Figs. 7, 8, and 9, respectively.
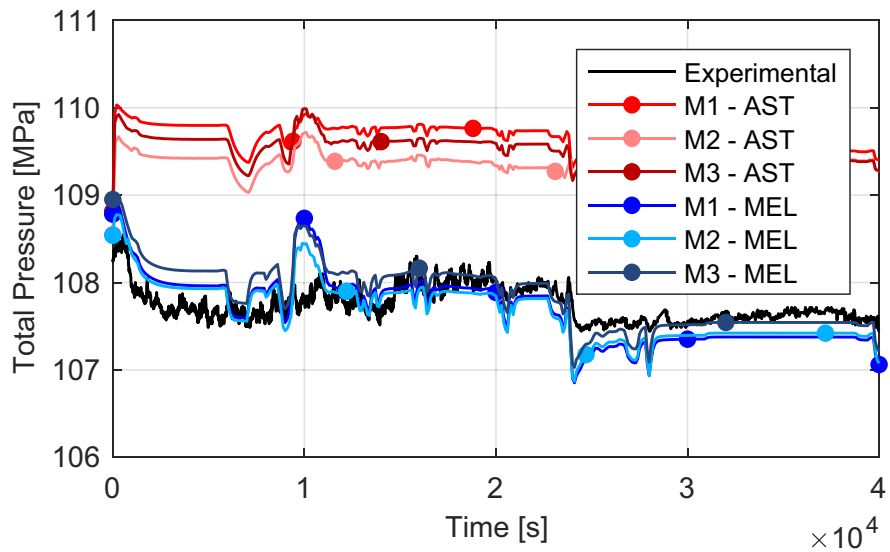
Fig. 7. Atmospheric temperature evolution at 2.32 m during the degradation phase.
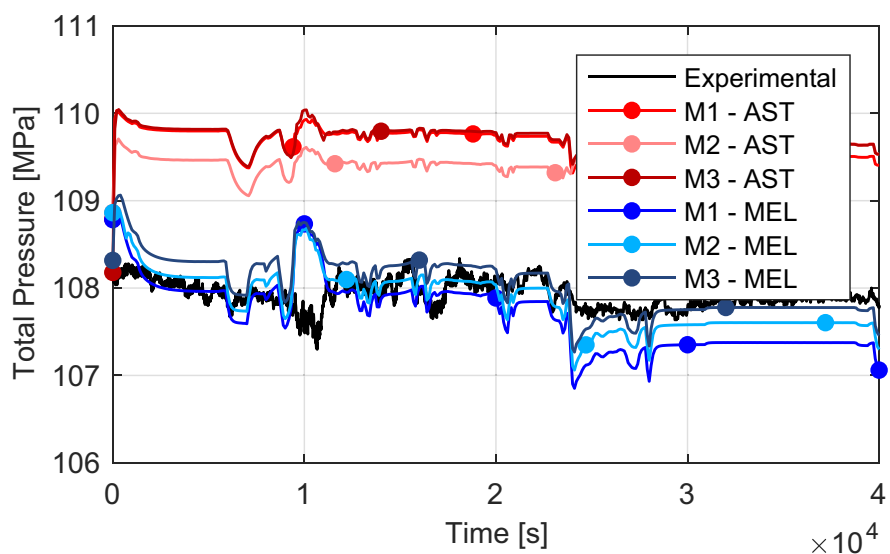
Fig. 8. Atmospheric temperature evolution at 3.0 m during the degradation phase.
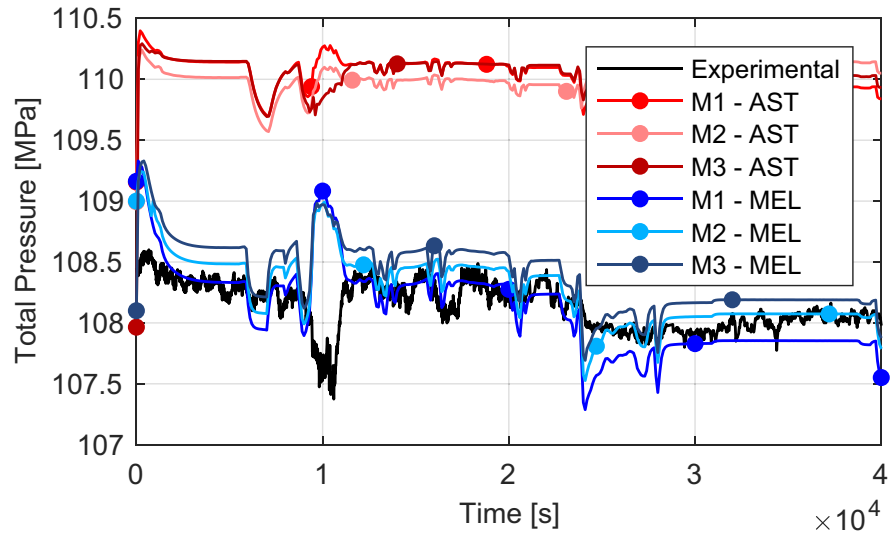
Fig. 9. Atmospheric temperature evolution at 4.02 m during the degradation phase.

Differences exist among the codes and the three employed nodalizations, but the maximum difference does not exceed 2 °C. This small value can be considered fully acceptable, and it is comparable to the values shown in previous works [11, 12, 13, 14, 15, 30, 31].

In Figs. 10, 11, and 12 the atmospheric temperatures between 40,000 s (11.11 h) and 200,000 s (55.56 h) at an elevation of 2.32 m, 3.0 m, and 4.02 m are reported. During this aerosol phase, the maximum discrepancy is shown by ASTEC at 4.02 m (3 °C). In turn, the following washing phase is well predicted only by ASTEC, except at 4.02 m where an error of about 7 °C is shown. In MELCOR, the atmospheric
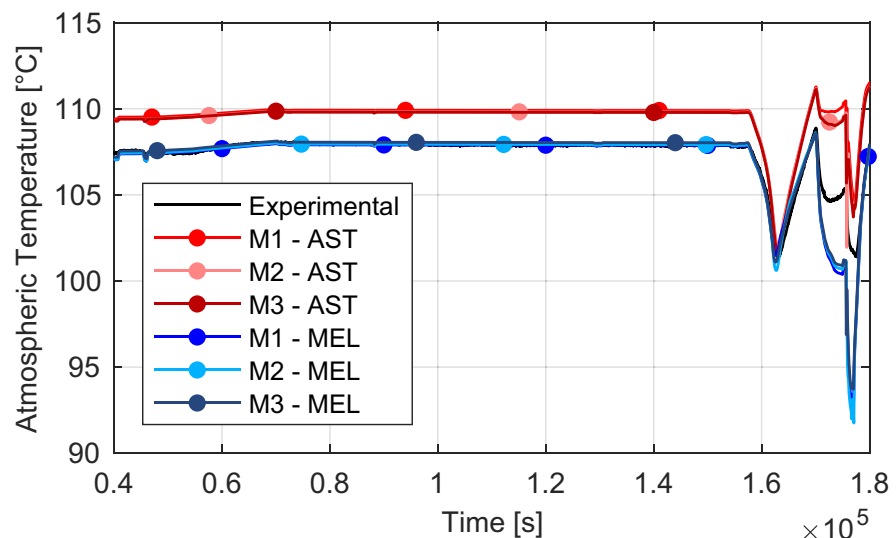

Fig. 10. Atmospheric temperature evolution at 2.32 m during the aerosol, the washing, and the early chemistry phases.
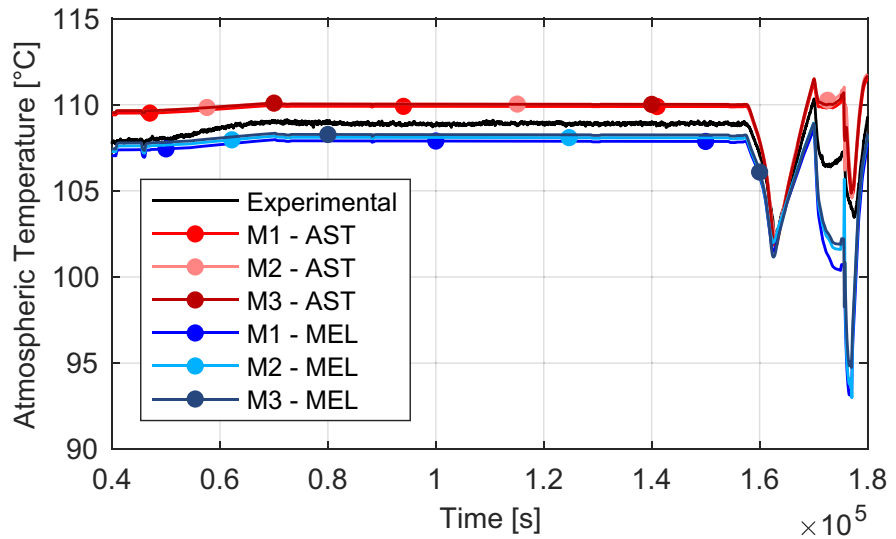
Fig. 11. Atmospheric temperature evolution at 3.0 m during the aerosol, the washing, and the early chemistry phases.

temperatures at 2.32 m and 4.02 m decrease 13 °C below the experimental ones once the sprays system is activated. Finally, during the chemistry phase (Fig. 13 refers to 2.32 m) a mean error lower than 2 °C is shown for both codes. The poor MELCOR predictions led to the execution of a sensitivity study discussed in the following "thermal-hydraulics sensitivity analyses" section.

In Fig. 14 the relative humidity evolution during the entire test is reported. During the initial degradation phase maximum errors of about 4% and about 8% are shown
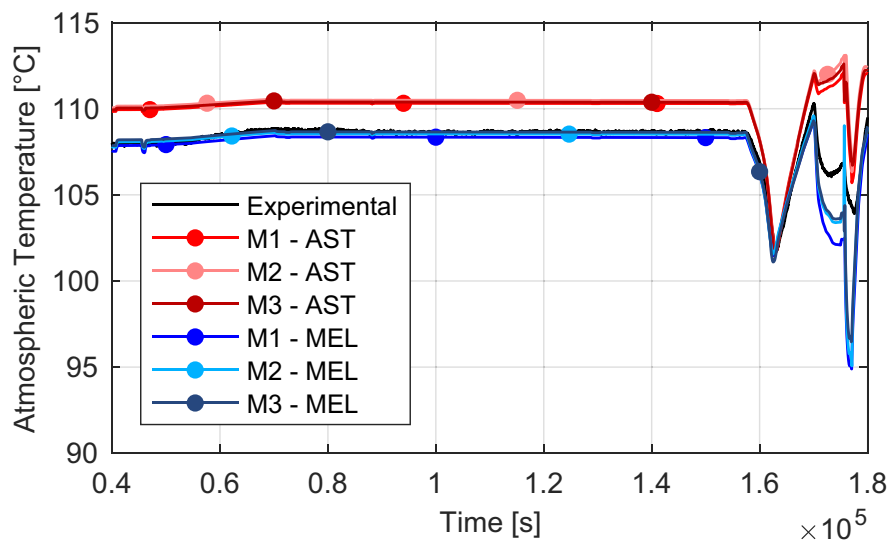

Fig. 12. Atmospheric temperature evolution at 4.02 m during the aerosol, the washing, and the early chemistry phases.
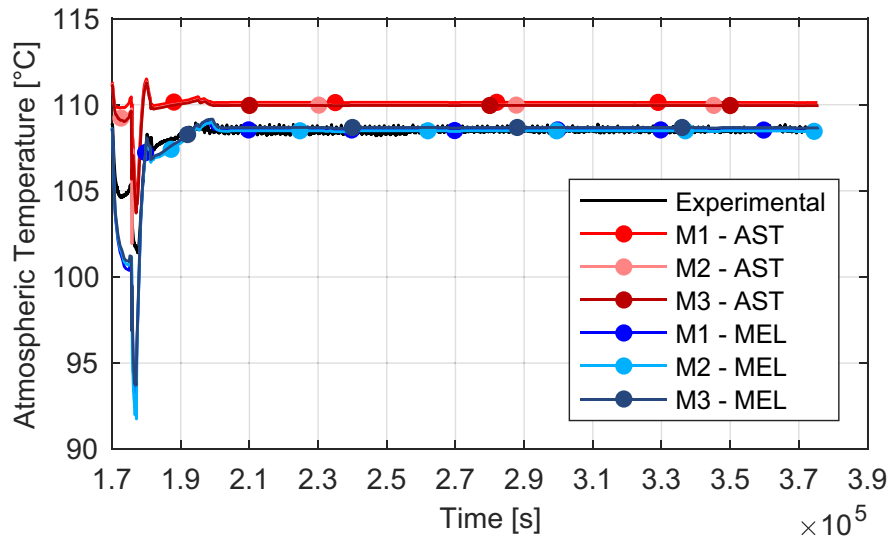
Fig. 13. Atmospheric temperature evolution at 2.32 m during the chemistry phase.

by MELCOR and ASTEC, respectively. In the following aerosol phase, the r.h. predictions are quite poor as discussed before, while in the washing and the chemistry phases good predictions are shown again. Although, during the spray operation, a partial evaporation of the water droplets is predicted, leading to a r.h. spike which is not present in the experimental data.

In Fig. 15 the total condensation rate onto the wet condenser surfaces is reported. The results obtained employing both codes follow the experimental results except between 9,500 s (2.64 h) and 11,000 s (3.06 h), i.e. just after an important ingress
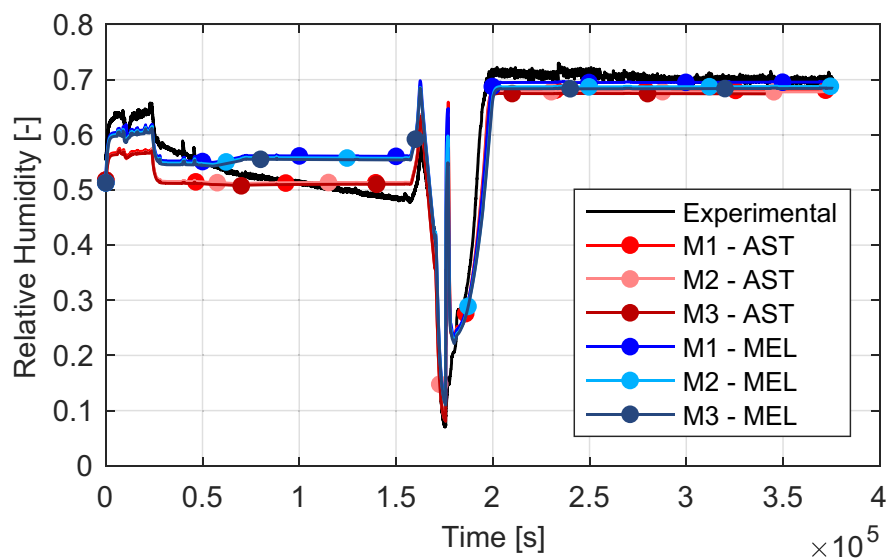

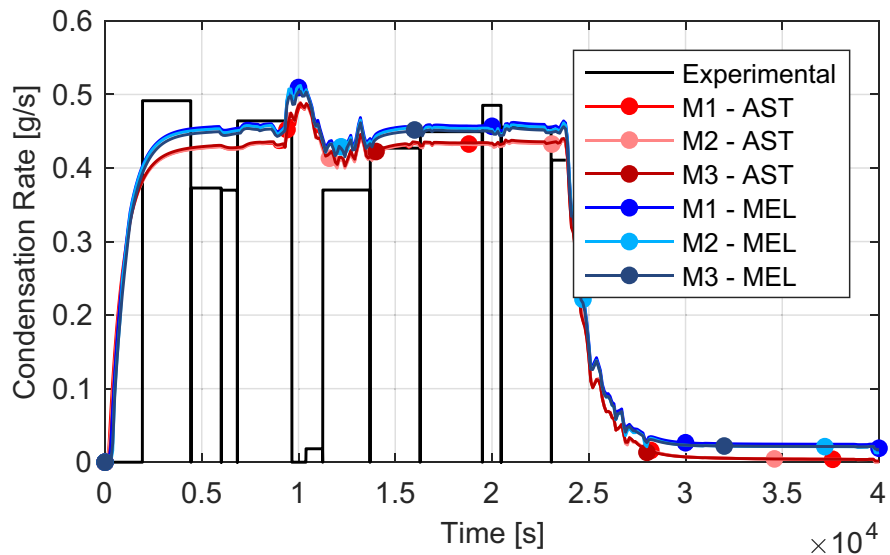**Fig. 14.** Relative humidity evolution during the entire test.

Fig. 15. Total condensation rate onto the wet condenser surfaces during the degradation phase.

of H_2 in the CV. Probably, in this time window, the H_2 plume creates an atmosphere poor in steam near to the condenser zone, thus a reduction of the condensation occurs due to the lack of steam. These local phenomena can be reproduced only by very detailed nodalizations, as shown for the THAI tests [32]. The obtained results suggest that initially the injected H_2 stops below the wet condensers, enhancing the transport of steam onto the wet condensers thus enhancing the predictions of the condensation rate. No experimental data are reported after 23,500 s (6.53 h) in [10], but the overall condensation rate trend is well predicted by both codes until this instant. Although, even if the condensation rate is well captured, differences exist among the experimental r.h. evolution and that predicted by both codes (Fig. 6). Finally, in Fig. 16 the water sump temperature evolutions are reported. Except during the spray operation time window, the predictions well agree with the experimental data. Maximum overestimation of about 10 °C and 25 °C are shown by MELCOR and ASTEC, respectively, during this spray operation phase. In the following chemistry phase a small difference of 3−4 °C exists between the experimental data and the code predictions.

The results shown in this section highlight that no major differences exist among the three developed CV nodalizations. Important differences only appear for the atmospheric temperatures during the washing phase and at the beginning of the chemistry phase, but these differences only last for a short time period compared to the extent of the test. For this reason, there are no motivations to choose the most complex nodalization looking exclusively at the thermal-hydraulic results. Although, this is not the case for the coupling of the thermal-hydraulic transient and the aerosol behavior. In the following section, more details on this coupled analysis are provided.
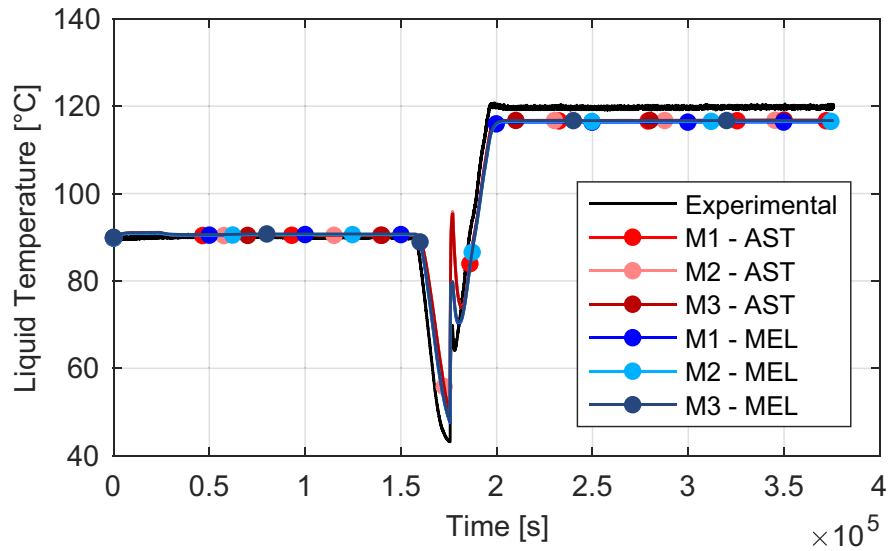
Fig. 16. Sump water temperature evolution during the test.

4.2. Thermal-hydraulic sensitivity analyses

The poor atmospheric temperatures predictions by MELCOR during the washing phase had led to thorough sensitivity analyses to improve the FPT-2 test predictions. On the contrary, such analyses were not carried out for ASTEC because acceptable values were obtained employing the standard input decks. Similar issues were also found in the analysis of the Phébus FPT-0 test [19]. As for the FPT-0 test, the CL values of the CV outer surfaces were found to be the most influencing parameter. For this purpose, a careful analysis was carried out to find the CL values better reproducing the thermal-hydraulic transient. This analysis has been carried out substituting the default CL values (Tables 3, 4, and 5) calculated for the different outer wall structures with values spanning from 0.01 m to 0.1 m. Common values were imposed for each outer vessel structure, and a try-and-check approach was followed to find the value better reproducing the thermal-hydraulic transient in each developed nodalization.

For each nodalization, different CL values have been found to better reproduce the thermal-hydraulic transient: 0.02 m provided exhaustive results in M1, 0.015 m in M2, and 0.08 m in M3. Compared to M1, M2 needs a smaller CL value while

Table 3. Characteristic lengths of the HS composing Model 1.

Model 1

HS name	WSU	WB1	W3	W4	W2T	W4T	WET	DRY
Characteristic length [m]	0.146	0.416	2.299	1.007	0.146	0.416	0.15	0.15

Table 4. Characteristic lengths of the HS composing Model 2.

Model 2

Name	Characteristic length [m]
WSU	0.146
WB1	0.416
W7	0.759
W8	0.759
W9	0.782
W10	0.504
W11	0.504
W6T	0.146
W12T	0.416
WET4	0.15
WET5	0.15
WET6	0.15
DRY	0.15

M3 a higher one. The cause of this peculiar result isn't clear, but a combined increase of the vertical and radial subdivision may be the cause. In Figs. 17, 18, and 19 the improvements obtained for the M3 case with this new CL value (0.08 m) are reported. The total pressure predictions are almost identical to the default ones, while

Table 5. Characteristic lengths of the HS composing Model 3.

Model 3

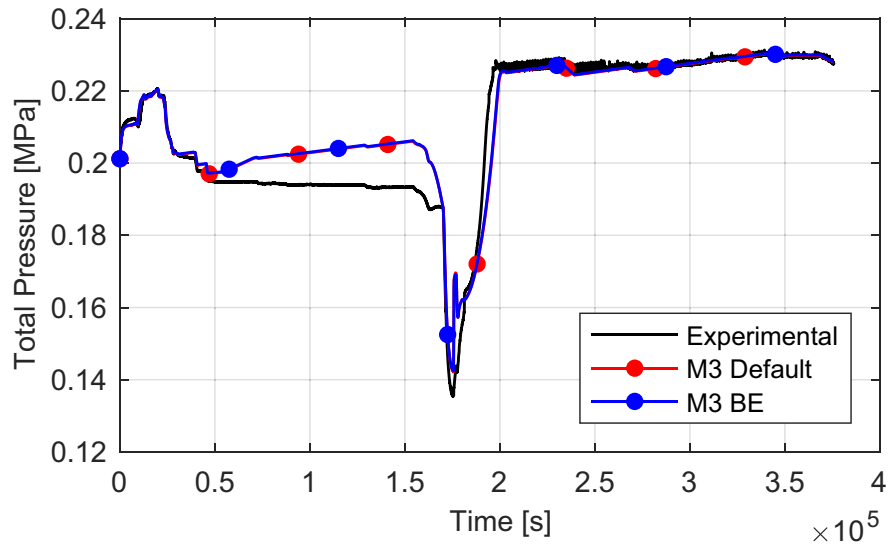| Name	Characteristic length [m]
WSU	0.146
WB1	0.265
WB2	0.142
W13	0.759
W14	0.759
W15	0.782
W16	0.504
W17	0.504
W6T	0.146
W12T	0.265
W18T	0.142
WET4	0.15
WET5	0.15
WET6	0.15
DRY	0.15

Fig. 17. Differences in the total pressure evolution among the MELCOR M3 default and BE cases.

the atmospheric temperature values during the aerosol, washing, and chemistry phases are now slightly closer to the experimental ones. Although, the improved atmospheric temperature estimations lead to a slightly worse r.h. prediction (in the order of 1−2%).

The heat transfer models implemented in MELCOR can be blamed for the poor prediction during the washing phase. As stated in [28], the heat transfer regime is defined in the code basing on the ratio between the Reynolds (Re) and the Grashof
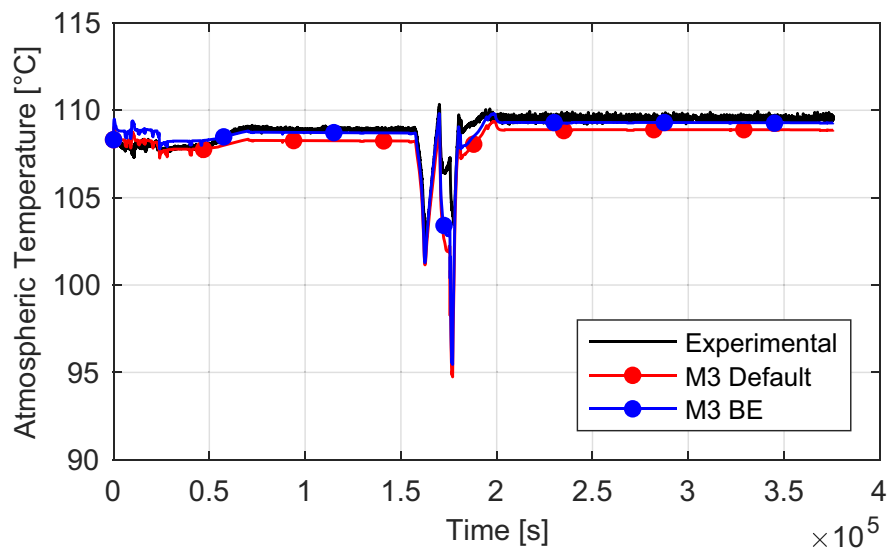

Fig. 18. Differences in the atmospheric temperature evolution at 3.0 m among the MELCOR M3 default and BE cases.
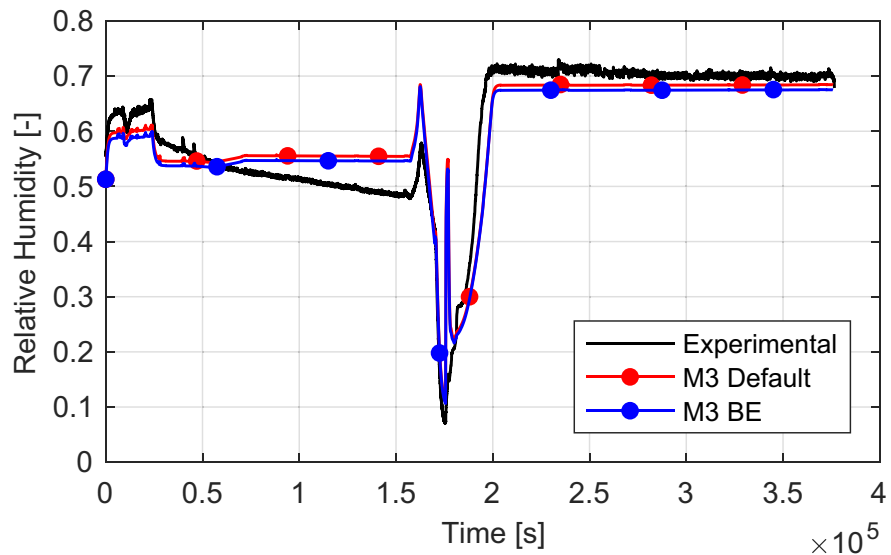
Fig. 19. Differences in the relative humidity among the MELCOR M3 default and BE cases.

(Gr) numbers. When the ratio Re^2/Gr is below 1 a natural convection regime is considered, if above 10 a forced convection regime is established, and an intermediate condition is considered in between. The Re number varies linearly with CL, while the Gr number with a cubic-power dependency, thus the Gr number decreases faster than the Re number if lower CL values are employed and all the other parameters are kept constant. Hence, the ratio Re^2/Gr will increase as the considered CL value decreases, meaning that the thermal-hydraulic conditions will move from a natural convective regime to an intermediate or even to a full forced convection regime. Because of this, the heat transfer coefficient calculated by MELCOR will increase as the employed CL value decreases. Similar conclusions were also found for the Phébus FPT-0 test [19]. The important influence of the CL was also stressed in [33], where a study on the influence of the CL value on the heat transfer and condensation rates for vertically-oriented plate HSs was performed. Even if different walls geometries were considered in the present work (vertical cylinders instead of vertical plates), a connection exists between the two works.

4.3. Aerosol and fission product results

As stated in the thermal-hydraulic results section, only minor differences are shown among the results obtained with the three employed spatial nodalizations. Therefore, the aerosol and FP behavior have been preliminarily investigated employing the CV different models. From this preliminary analysis, it was found that only the third spatial nodalization (M3) is able to correctly predict the coupling between the thermal-hydraulics transient and the aerosols and FP behavior. For this reason, in the following only the results obtained with the M3 model will be discussed. All

the chemical elements reaching the CV have been simulated, but the following discussion will focus only on the main FP and on structural materials. The aerosol behavior was found to be almost identical in MELCOR M3 default and previous best-estimate case, so in the following only the default case results will be shown and discussed.

In Fig. 20 the evolutions of the suspended and deposited aerosol masses are reported. The two codes produce different results, both characterized by a faster FP deposition than the experimental one due to the overestimation of the magnitude of the agglomeration and deposition processes. In Fig. 21 the atmospheric iodine mass is reported. The main drawback of this analysis is the absence of information regarding the evolution of the dose rate inside the CV [10]. For this reason, dose rates in atmosphere and sump were not provided in the two input decks, and the iodine oxides "formation and destruction" cycle, characterizing the iodine behavior in containment [34], was not captured by both codes. Thus, the poor evolution shown by both codes is not strictly related to their modelling approaches. In turn, the iodine mass deposited onto the wet condenser surfaces should be better estimated because it manly depends by the local thermal-hydraulic conditions. The results reported in Fig. 21 show that in ASTEC the deposition process onto the wet condenser surfaces is well captured, while in MELCOR the iodine does not deposit on the condenser surfaces because it is trapped in the water film which flows into the sump. This MELCOR behavior is not due to a user's assumption, but it is the normal behavior of the water-film tracking model as explicitly declared by the sensitivity coefficient no. 7136 (solubility of RN classes in water films) [16]. This value can be changed, but no sensitivity analyses have
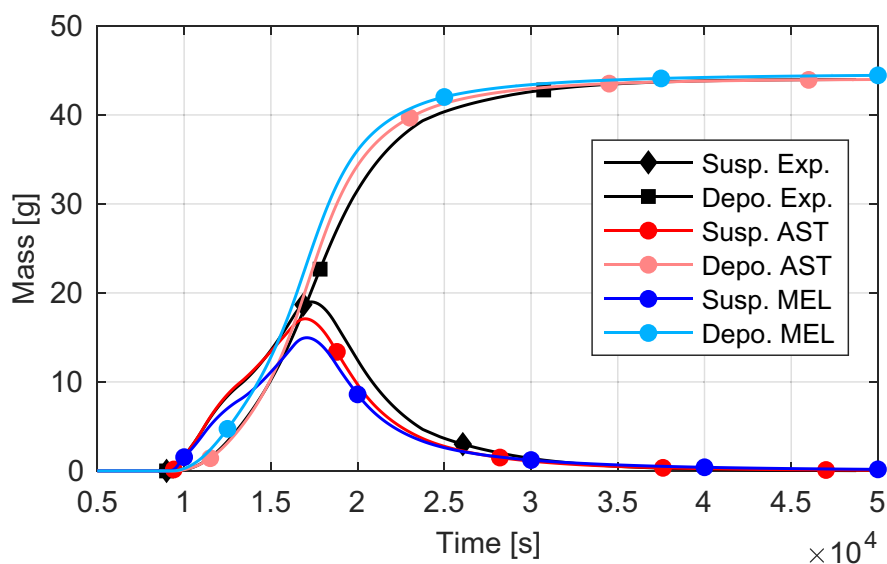

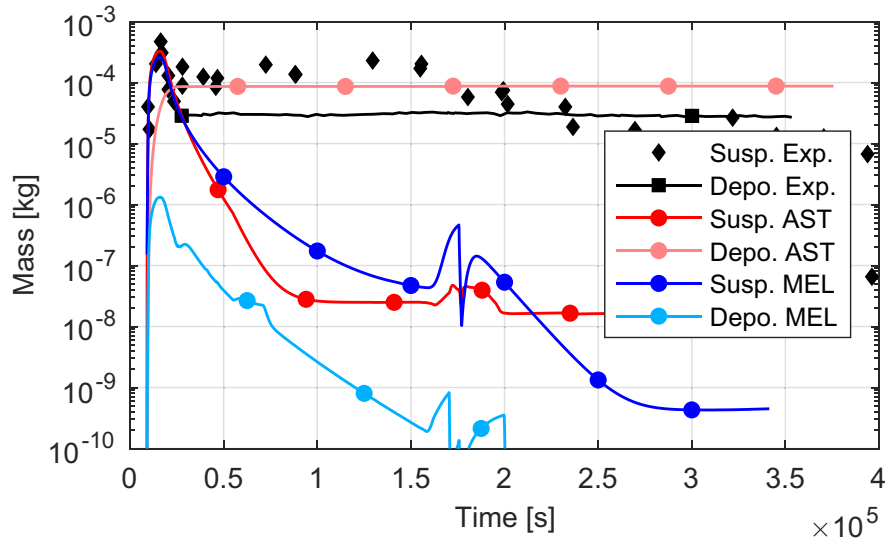**Fig. 20.** Atmospheric and deposited aerosol mass.

Fig. 21. Evolution of the atmospheric iodine and the deposited iodine onto the wet condenser surfaces.

been performed due to the absence of information on the repartition coefficient between the film and the structure.

The evolution of the iodine masses in the sump is reported in Figs. 22 and 23 for ASTEC and MELCOR, respectively. The reaction rates and the partition coefficients between water and atmosphere were computed by the two codes according to the local thermal-hydraulic conditions. Although, even if the thermal-hydraulic predictions were quite similar in both codes, significant differences exist in the iodine speciation during the test. For the ASTEC code, iodine stays mainly I^- and AgI,
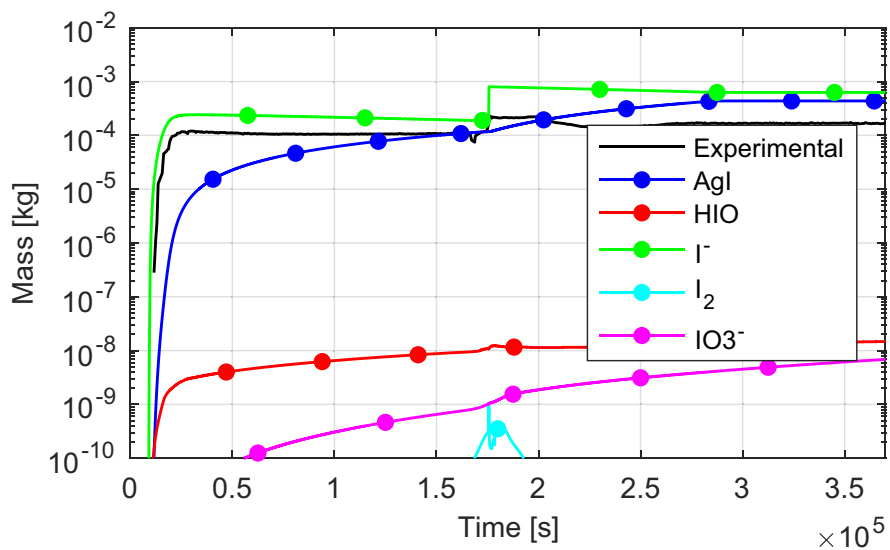

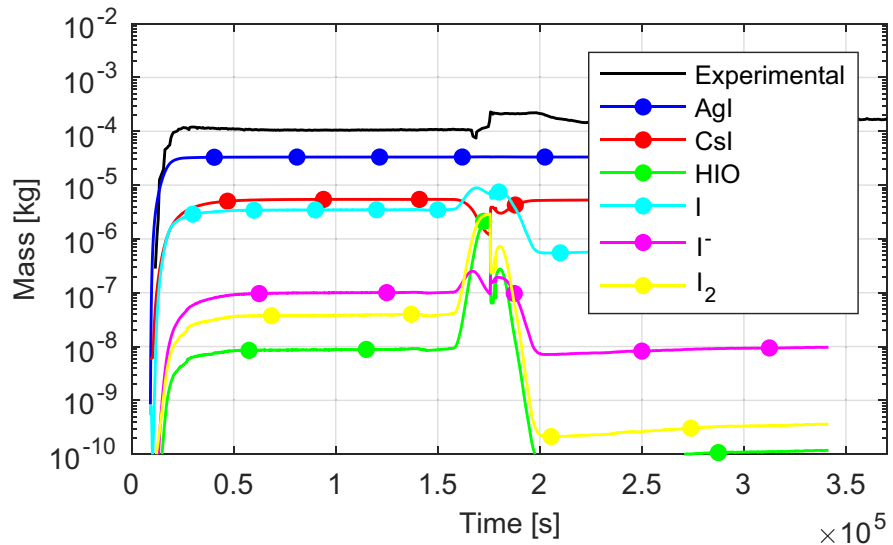**Fig. 22.** Iodine speciation in the sump water (ASTEC).

Fig. 23. Iodine speciation in the sump water (MELCOR).

because the Ag depositing in the sump is not sufficient to capture the whole I_2 sump inventory (0.9 of I_2 and 7 g of Ag flows into the CV), and the remaining I_2 is dissociated into I^- ions. The total I_2 amount flowing inside the sump is slightly higher than the experimental predicted amount. This discrepancy surely leads to an overestimation of I^- ions production, but the real magnitude of this phenomenon cannot be estimated.

The MELCOR predictions are quite different from the ASTEC ones, but some similarities can be identified:

- For MELCOR the iodine is mainly in three forms (AgI, CsI, and I^-) instead of two as for ASTEC (I^- and AgI). Again, iodine in the sump is mainly bound by Ag, and the remaining I_2 is rapidly transformed in CsI and I^-.

- The speciation into other iodine forms is less important for both codes, but significant differences exist. For ASTEC iodine is partially transformed in HIO and IO_3^-, while for MELCOR iodine remains mainly I_2 and HIO.

On the contrary, the main differences between the ASTEC and MELCOR predictions are:

- For MELCOR the iodine mass flowing into the sump is slightly underestimated compared to the experimental data. This result, in addition to the poor estimation of the iodine deposited onto the wet condenser surfaces, led to the conclusion that the iodine deposition onto the CV vertical walls and on the bottom semiellipsoidal structure is overestimated.

- After the spray activation, iodine and the other FP deposited onto the bottom semi-ellipsoidal structure are transported inside the sump. For ASTEC the ingress of iodine and Ag in the sump trigger the formation of new AgI, and in minor extent of IO_3^-. On the contrary, for MELCOR the iodine washed away is partially transported into the sump and partially released back into the CV atmosphere (Fig. 21). Moreover, in the sump the CsI amount decreases and I^-, I_2, and HIO compounds are formed, but almost all the transformed iodine returns again as CsI once terminated the washing phase. The AgI evolution seems not influenced by the transformation of all the other iodine forms, but it should be also considered that the total mass of I^-, I_2, and HIO is almost negligible compared to that of AgI.

To conclude, it can be stated that the aerosol and FP results are not satisfactory due to the lack of information about the dose rates in the CV atmosphere and in the sump. In future analysis, this issue should be addressed to provide more exhaustive results.

4.4. Aerosol and fission product sensitivity analyses

The influence of different input parameters has been investigated through a quite large execution of sensitivity analyses for both codes. In MELCOR no differences were shown between the default case and that developed for the thermal-hydraulic sensitivity case, thus in the following only the results of the default case will be reported.

The main input parameters implemented in both codes that have a substantial influence on the predictions are:

- **Dynamic shape factor for agglomeration processes.** A default value of 1 is suggested for both codes [16, 25], and three additional sensitivity analyses have been performed setting this parameter to 1.5, 2 and 3. Each value means that the particles have different geometries: 1 means that are spherical, 1.5 that are similar to sand, and 2 means that are similar to talc powder [35]. In Figs. 24 and 25 the effects on the total deposited mass in MELCOR and ASTEC are shown. In MELCOR, a value of 2 provides more exhaustive results, while in ASTEC the default value (1) seems the best one. Previous analyses [30] also suggested the same conclusions.

- **Aerosol density.** No experimental data nor default values were provided for the aerosol density, but values spanning from 3,000 kg/m^3 to 10,000 kg/m^3 were suggested in previous works [12, 13, 14]. In the present paper, five sensitivity cases were investigated setting the density value to 1,000 kg/m^3 (default MELCOR value for wet aerosol particles [16]), 3,000 kg/m^3 (default case), 10,000 kg/m^3, 15,000 kg/m^3, and 20,000 kg/m^3. The default aerosol density assumed
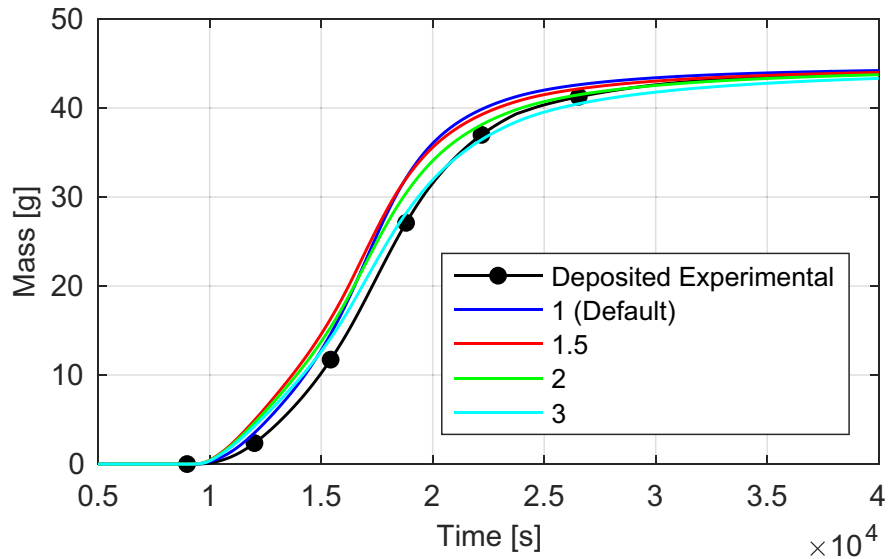
Fig. 24. Results of the MELCOR sensitivity analyses on the dynamic shape factor − total deposited aerosol mass.

(3,000 kg/m^3) was inferred from the previous cited works. This parameter was found to provide similar effects in both codes: the increase of the aerosol density increases the magnitude of the deposition processes (Figs. 26 and 27), leading to a too fast FP depletion in the atmosphere. The reduction of the aerosol density has the opposite effect, but again the results are partially incongruent with the experimental ones due to the slow FP depletion computed.
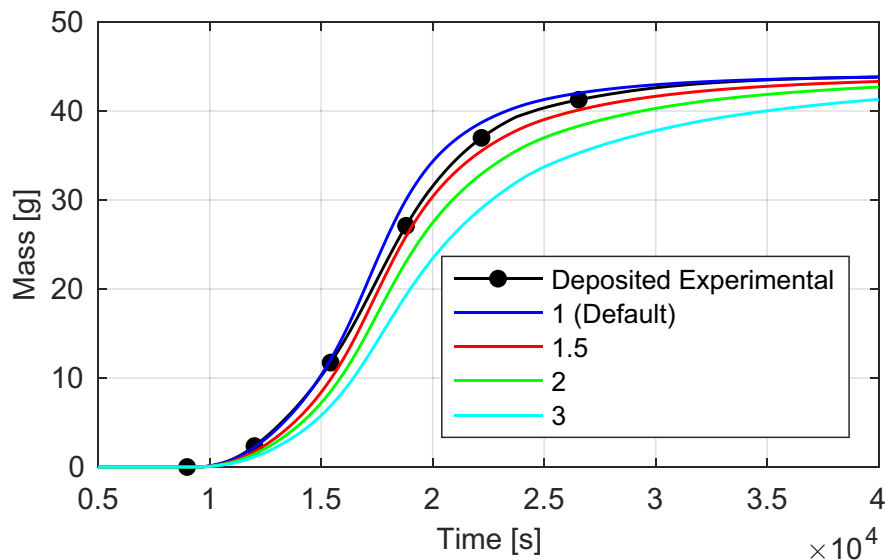

Fig. 25. Results of the ASTEC sensitivity analyses on the dynamic shape factor − total deposited aerosol mass.
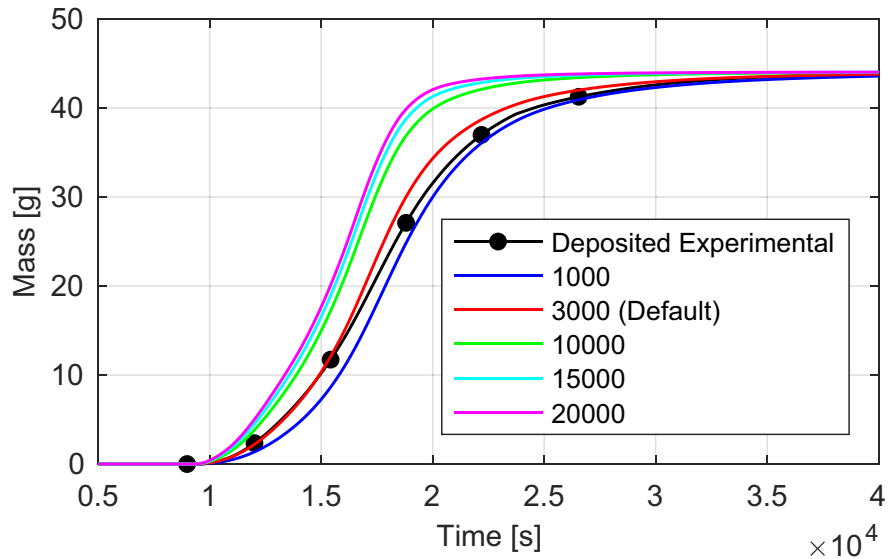
Fig. 26. Results of the ASTEC sensitivity analyses on the aerosol density – total deposited aerosol mass.

- **Agglomeration shape factor.** A default value of 1 is suggested for both codes [16, 25], but three additional sensitivity analyses have been executed setting this parameter to 0.5, 2, and 3. The effects on the ASTEC and MELCOR calculations are the same of those shown for the aerosol density, but in this case an agglomeration factor set to 0.5 in ASTEC provides results closer to the experimental data (Fig. 28).
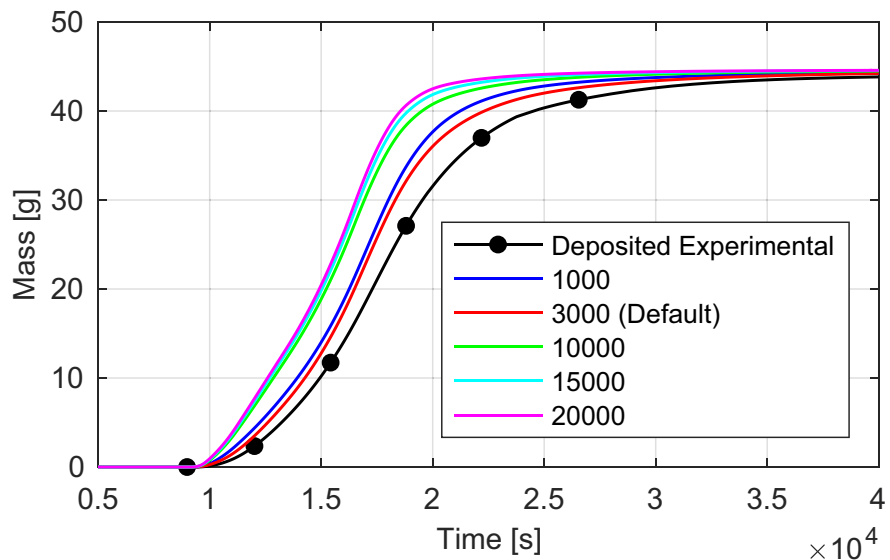

Fig. 27. Results of the MELCOR sensitivity analyses on the aerosol density – total deposited aerosol mass.
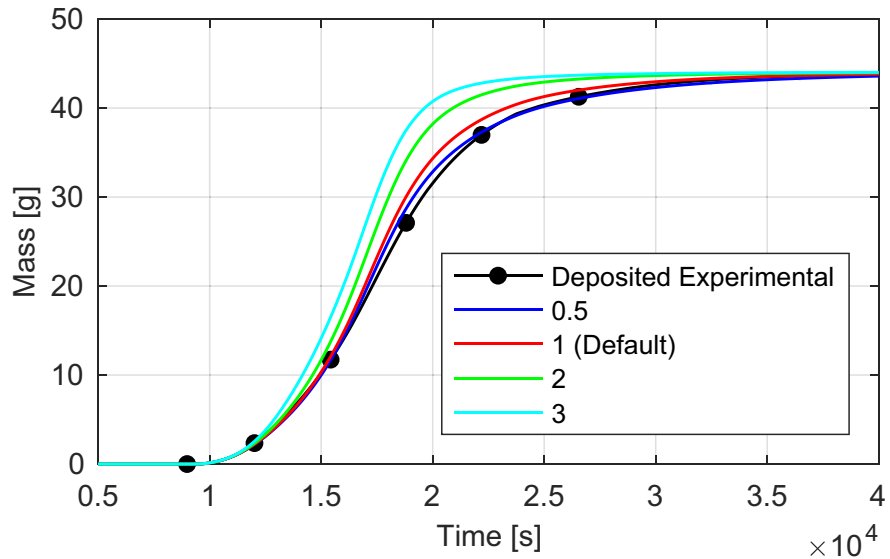
Fig. 28. Results of the ASTEC sensitivity analyses on the agglomeration shape factor − total deposited aerosol mass.

- **Particle sticking probability.** A default value of 1 is suggested [16, 25], and three additional sensitivity cases have been investigated setting this parameter equal to: 0.5, 2, and 3. In ASTEC almost negligible differences are present among the different cases, while in MELCOR (Fig. 29) slightly better results are obtained with a particle sticking probability set to 0.5, but a too strong deposition is still predicted.
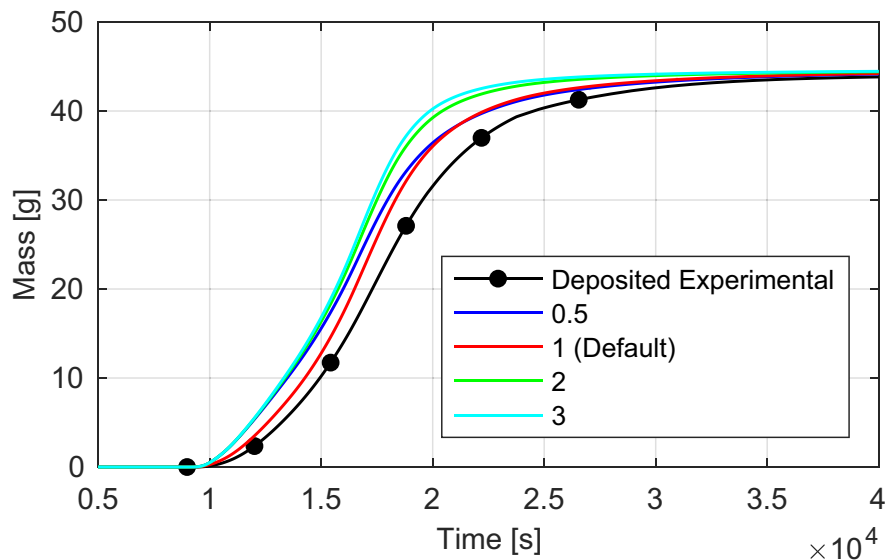
Fig. 29. Results of the MELCOR sensitivity analyses on the particle sticking probability − total deposited aerosol mass.

- **AMMD and GSD.** Mean AMMD and GSD values for the main element compounds were provided in [10], but no information on their uncertainties was reported. For this reason, four sensitivity analyses were carried out increasing or decreasing the AMMD or the GSD values by 25% respect to the specification values. A modification on the GSD value provides negligible effects, while the modification of the AMMD has a greater impact due to the influence on the different agglomeration phenomena. In both codes (Figs. 30 and 31) an

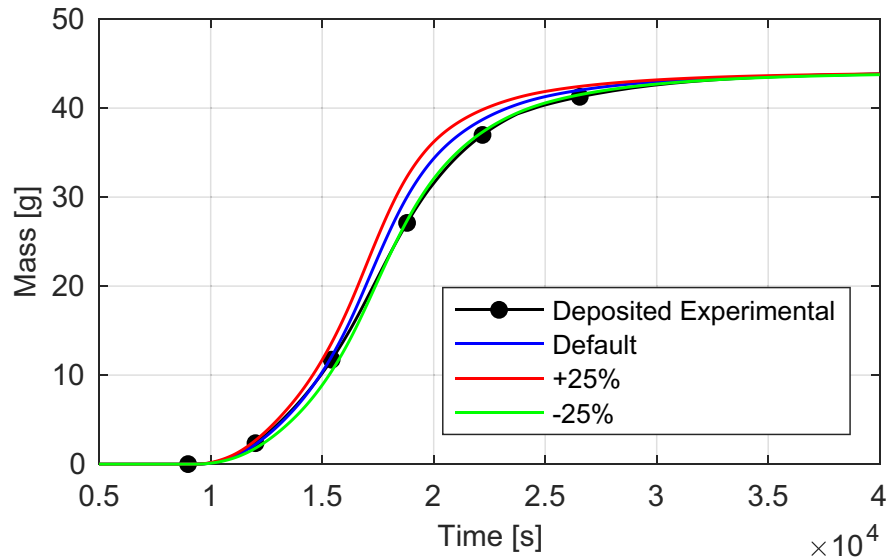Fig. 30. Results of the MELCOR sensitivity analyses on AMMD − total deposited aerosol mass.
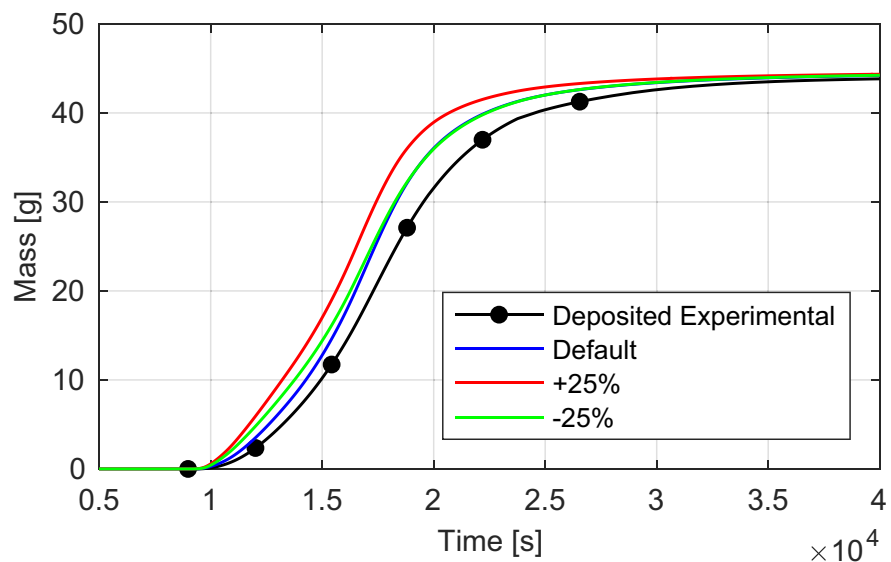

Fig. 31. Results of the ASTEC sensitivity analyses on AMMD − total deposited aerosol mass.

AMMD value set to -25% of the default value has provided more exhaustive results, especially in ASTEC.

Finally, the parameters described in Table 6 were investigated with both codes, but they didn't show up any important influence on the calculation results.

Both codes implement other specific input parameters. Some of these parameters were investigated, but in ASTEC none of these specific input parameters have been found to influence the calculations, while in MELCOR only the "Partition of I- and HIO between atmosphere and sump" has been found to play a minor role. In the default case the partitioning for both components is deactivated (as suggested by MELCOR User's Guidelines [16]), but two sensitivity cases have been performed, selectively activating the I^- and the HOI partitioning. The activation of I^- partitioning has reported a numerical instability after the washing phase, thus the run was aborted. On the contrary, the activation of HIO partitioning (Fig. 32) runs fine, and it led to a slightly increase of the atmospheric iodine, but the predicted masses were still two orders of magnitude below the experimental ones.

In Tables 7 and 8 are reported the other specific parameters investigated with the ASTEC and the MELCOR codes, respectively.

Table 6. Sensitivity parameters investigated with both codes.

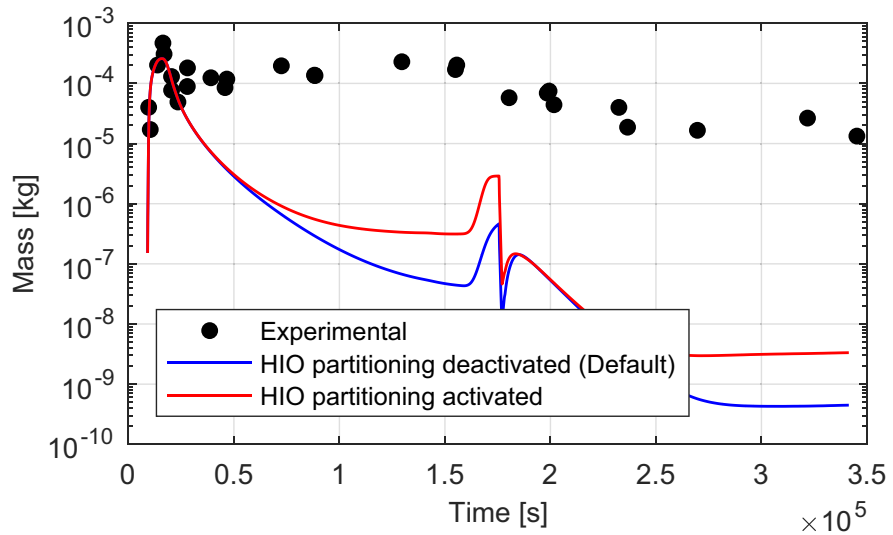| Parameter	Description	Values investigated	Comments
Number of Particle Size Classes	The number of intervals (classes) in which the distribution of the injected aerosols is subdivided.	10 (default MELCOR) 20 30 40 50	The default value employed is 20, as did in previous works [13, 14, 30].
Turbulence dissipation rate [m^2/s^3]	\	0.001 (default MELCOR) 0.005 0.01 0.02 (default ASTEC) 0.03	Negligible influence in ASTEC, and slightly better results in MELCOR with a value of 0.001 m^2/s^3. The use of their respective default values may be suggested.
Ratio of the thermal conductivity of the gas phase to the thermal conductivity of the aerosol particles [W/mK]	\	0.05 (default ASTEC) 0.005 (default MELCOR) $5.0 \cdot 10^{-4}$ $5.0 \cdot 10^{-5}$	No influence at all.

Fig. 32. Effect of HOI partitioning on the calculated iodine atmospheric mass.

Table 7. Sensitivity parameters investigated with the ASTEC code.

Parameter	Values investigated	Comments
Influence of the aerosol particles on the gas density	"on" "off" (default)	\
Dynamic calculation of the condensation time step [N/m]	0.0586 (100 °C default) 0.0598 (95 °C) 0.0572 (105 °C) 0.0559 (110 °C)	Five cases investigated changing the surface tension of a droplet in the atmosphere These five values refer to different droplet equilibrium temperatures (show in parenthesis).
Air molecular weight [kg/mol]	23.5 (air - default) 28.96 (100% N_2) 18.02 (100% O_2) 20.76 (50 N_2 − 50 O_2)	Each value investigated refers to a different air composition.
Relation for the calculation of the collision efficiency for gravitational and turbulent coagulation	Pruppacher-Klett (default) Fuchs Truncated Pruppacher-Klett	\
Thickness of water film used for drainage of and aerosol wash-down [mm]	1 0.1 (default) 0.01	\
Aerosol deposition velocity for each aerosol component [mm/s]	0 (default) 10 1 0.1	\

Table 8. Sensitivity parameters investigated with the MELCOR code.

Parameter	Values investigated
Condensation of water on all the aerosol particles, or only on the aerosol particles containing water	"all" (default) "only with water"
Particle slip coefficient influencing the gravitational deposition	1 1.257 (default) 1.5 2
Constant associated with the thermal accommodation coefficient for thermophoresis deposition	1 2 2.25 2.5 3
Diffusion boundary layer thickness [mm]	0.1 0.5 0.01 (default) 0.05 0.001

Table 9. Summary of the sensitivity cases performed, and importance for the ASTEC and MELCOR results.

Parameter	Importance for ASTEC calculations	Importance for MELCOR calculations
I^- partitioning among sump water and atmosphere	╲	(Numerical instabilities)
HIO partitioning among sump water and atmosphere	╲	**High**
Aerosol deposition velocity for each aerosol component	Low	╲
Dynamic shape factor for agglomeration processes	**High**	**High**
Collision efficiency for gravitational and turbulent coagulation	Low	╲
Aerosol density	**High**	**High**
Dynamic calculation of the time-step + Surface tension of a droplet in the atmosphere	Low	╲
Agglomeration shape factor	**High**	**High**
Consideration of the aerosol particles presence for calculating the gas density	Low	╲
Number of particle size classes	Low	Low
Aerodynamic mass median diameter	**High**	**High**
Geometric standard deviation	Low	Low
Particle sticking probability	Low	**High**
Thickness of water film used for drainage and aerosol wash-down	Low	╲
Thermal conductivity of gas divided by thermal conductivity of aerosol particle	Low	Low
Turbulence dissipation rate	Low	**High**
Molecular weight of gas.	Low	╲
Diffusion boundary layer thickness	╲	Low

(continued on next page)

Table 9. (*Continued*)

Parameter	Importance for ASTEC calculations	Importance for MELCOR calculations
Thermal accommodation coefficient	╲	Low
Particle slip coefficient	╲	Low
Condensation onto wet aerosols	╲	Low

5. Conclusions

In the present paper, a comparison between the ASTEC and MELCOR codes against the results for the containment aspects of the Phébus FPT-2 test has been performed. Three spatial nodalizations of the CV have been employed to investigate the coupling between the thermal-hydraulic transient and the aerosol behavior. These nodalizations have been developed in the closest way possible for both codes, but the different modelling approaches of certain aspects were all exploited to show the capabilities of each code.

From the stand-alone thermal-hydraulic analysis, it was found that no motivations exist to choose the most complex CV nodalization, but the coupled analysis showed the need for a sufficiently refined geometrical schematization.

The most complex spatial nodalization (M3) has shown acceptable thermal-hydraulic results, even if some discrepancies with the experimental data exist. These discrepancies are mainly introduced by user's assumptions, such as during the time window of the preparatory actions before the washing phase, and during the beginning of the chemistry phase. Such effects mainly affect the atmospheric temperature predictions, which in turn influence the CV total pressure and the r.h. results.

The aerosol behavior is mainly influenced by the thermal-hydraulics conditions during the early 50,000 s (13.89 h) of the test, and the exhaustive results shown during this time interval demonstrate that the thermal-hydraulics predictions are good enough. In some cases, the sensitivity analyses performed have shown that the default parameters employed for the aerosol behavior estimation were not able to predict at the best the experimental trends. In ASTEC an agglomeration factor set to 0.5 instead of 1 may be suggested, as well as the increase to 2 of the dynamic shape factor in MELCOR. Other parameters, as the aerosol density, the AMMD, the particle sticking probability, have shown a great influence on the aerosol behavior, but the results obtained are poorer than that of the default cases. Regarding the thermal-hydraulic comparison between the MELCOR default case and best-estimate one, important differences were shown. The code predictions for the best-estimate case are slightly better, but a weak or absent influence was shown on the final aerosol behavior predictions. For this reason, it can be concluded that the improvements of the thermal-hydraulics predictions did not lead to significant

improvements in the results and this step could be avoided in future analysis. In Table 9 a summary of the performed sensitivity cases is reported.

Quite important differences were shown in the comparison of the two codes about the prediction of the iodine behavior in the sump. In ASTEC important AgI and I^- presences are reported during the entire test, while negligible amounts of other species are shown. In turn, in MELCOR an important formation of AgI and CsI is predicted, and a certain amount of I^- is still reported. Although, the presence of CsI does not reflect the actual state-of-the-art of iodine chemistry [18]. The complex iodine speciation is somewhat surprising, considering the absence of the dose rate as a boundary condition. Indeed, the speciation in the sump is mainly triggered by the thermal-hydraulics conditions and by the radiolysis. In the present analysis no dose rates were added to the atmosphere and to the sump water due to the absence of information in the FPT-2 Final Report [10]. This absence is probably the most significant drawback of the entire analysis. In future analyses, such information should be introduced, otherwise the results obtained will be again limited.

Declarations

Author contribution statement

B. Gonfiotti: Performed the experiments; Analyzed and interpreted the data; Wrote the paper.

S. Paci: Conceived and designed the experiments; Analyzed and interpreted the data; Contributed reagents, materials, analysis tools or data.

Funding statement

Competing interest statement

The authors declare no conflict of interest.

Additional information

No additional information is available for this paper.

References

[1] J.-P. Van Dorsselaere, A. Auvinen, D. Beraha, P. Chatelard, L.E. Herranz, C. Journeau, W. Klein-Hessling, I. Kljenak, A. Miassoedov, S. Paci,

R. Zeyen, Recent severe accident research synthesis of the major outcomes from the SARNET network, Nucl. Eng. Des. 291 (2015) 19−34.

[2] J.-P. Van Dorsselaere, T. Albiol, J.-C. Micaelli, Research on severe accidents in nuclear power plants, in: Nucl. Power - Oper. Saf. Environ., InTech, 2011, pp. 155−182. http://www.intechopen.com/books/nuclear-power-operation-safety-and-environment/research-on-severe-accidents-in-nuclear-power-plants.

[3] D. Jacquemain, Nuclear Power Reactor Core Melt Accidents, Current State of Knowledge, first ed., EDP Sciences, 2015. http://bookstore.edpsciences.com/en/product/77/9782759819300/Nuclear Power Reactor Core Melt Accidents.

[4] B. Clément, R. Zeyen, The objectives of the Phébus FP experimental programme and main findings, Ann. Nucl. Energy 61 (2013) 4−10.

[5] O. de Luze, M. Barrachin, G. Repetto, Early phase fuel degradation in Phébus FP: initiating phenomena of degradation in fuel bundle tests, Ann. Nucl. Energy 61 (2013) 23−35.

[6] F. Payot, P.D.W. Bottomley, Transport and deposition in the Phébus FP circuit, Ann. Nucl. Energy 61 (2013) 102−121.

[7] M. Laurie, P. March, B. Simondi-Teisseire, F. Payot, Containment behaviour in Phébus FP, Ann. Nucl. Energy 60 (2013) 15−27.

[8] P. March, B. Simondi-Teisseire, Overview of the facility and experiments performed in Phébus FP, Ann. Nucl. Energy 61 (2013) 11−22.

[9] G. Brillant, C. Marchetto, W. Plumecocq, Fission product release from nuclear fuel II. Validation of ASTEC/ELSA on analytical and large scale experiments, Ann. Nucl. Energy 61 (2013) 96−101.

[10] A.-C. Gregoire, P. March, F. Payot, G. Ritter, M. Zabiego, A. de Braemaeker, B. Biard, G. Gregoire, S. Schlutig, PHEBUS FP FPT2 Final Report, Saint-Paul-lez-Durance (F), 2008.

[11] G. Gyenes, L. Ammirabile, Containment analysis on the PHEBUS FPT-0, FPT-1 and FPT-2 experiments, Nucl. Eng. Des. 241 (2011) 854−864.

[12] L.E. Herranz, M. Vela-García, J. Fontanet, C.L. del Prá, Experimental interpretation and code validation based on the PHEBUS-FP programme: lessons learnt from the analysis of the containment scenario of FPT1 and FPT2 tests, Nucl. Eng. Des. 237 (2007) 2210−2218.

[13] A. Kontautas, E. Babilas, E. Urbonavičius, COCOSYS analysis for deposition of aerosols and fission products in PHEBUS FPT-2 containment, Nucl. Eng. Des. 247 (2012) 160−167.

[14] I. Kljenak, B. Mavko, Simulation of containment phenomena during the phe-bus FPT2 test with the CONTAIN code, in: Proc. Int. Conf. Nucl. Energy New Eur, 2009, pp. 417.1−417.8.

[15] I. Kljenak, M. Dapper, J. Dienstbier, L.E. Herranz, M.K. Koch, J. Fontanet, Thermal-hydraulic and aerosol containment phenomena modelling in ASTEC severe accident computer code, Nucl. Eng. Des. 240 (2010) 656−667.

[16] L.L. Humphries, R.K. Cole, D.L. Louie, V.G. Figueroa, M.F. Young, MEL-COR Computer Code Manuals Vol. 1: Primer and User's Guide Version 2.1.6840 2015, Albuquerque (USA), 2015.

[17] P. Chatelard, N. Reinke, S. Arndt, S. Belon, L. Cantrel, L. Carénini, K. Chevalier-Jabet, F. Cousin, J. Eckel, F. Jacq, C. Marchetto, C. Mun, L. Piar, ASTEC V2 severe accident integral code main features, current V2.0 modelling status, perspectives, Nucl. Eng. Des. 272 (2014) 119−135.

[18] B. Clément, L. Cantrel, G. Ducros, F. Funke, L.E. Herranz, A. Rydl, G. Weber, C. Wren, State of the Art Report on Iodine Chemistry, 2007.

[19] B. Gonfiotti, S. Paci, Stand-alone containment analysis of the Phébus FPT tests with the ASTEC and the MELCOR codes - the FPT-0 test, Sci. Technol. Nucl. Install. (2017). https://www.hindawi.com/journals/stni/aip/1450648/.

[20] B. Gonfiotti, S. Paci, Stand-alone containment analysis of the Phébus FPT-1 test with the ASTEC and the MELCOR codes, J. Nucl. Eng. Radiat. Sci. (2017).

[21] A. Kontautas, E. Urbonavičius, Analysis of aerosol deposition in PHEBUS containment during FPT-1 experiment, Nucl. Eng. Des. 239 (2009) 1267−1274.

[22] N. Hanniet-Girault, G. Repetto, FPT-0 Final Report, Saint-Paul-lez-Durance (F), 1999.

[23] D. Jacquemain, S. Bourdon, A. de Braemaeker, M. Barrachin, PHEBUS FPT1 Final Report, 2000.

[24] F. Payot, T. Haste, B. Biard, F. Bot-Robin, J. Devoy, Y. Garnier, J. Guillot, C. Manenc, P. March, PHEBUS FP FPT3 Final Report, Saint-Paul-lez-Durance (F), 2011.

[25] W. Klein-Hessling, B. Schwinges, ASTEC V0 CPA Module Program Refer-ence Manual, Institut de Protection et de Surete Nucleaire (IRSN - France)/ Gesellschaft fur Anlagen-und Reacktorsicherheit mbH (GRS - Germany), 1998.

[26] L. Bosland, ASTEC V2.0 rev2 Code IODE Module: Iodine and Ruthenium Behaviour in the Containment, Institut de Protection et de Surete Nucleaire (IRSN - France)/Gesellschaft fur Anlagen-und Reacktorsicherheit mbH (GRS - Germany), Saint-Paul-lez-Durance (F), 2011.

[27] G. Guillard, F. Jacq, C. Seropian, W. Plumecocq, ASTEC V1 Code SYSINT Module Management of Events and Safety Systems Interactions, Saint-Paul-lez-Durance (F), 2007.

[28] L.L. Humphries, R.K. Cole, D.L. Louie, V.G. Figueroa, M.F. Young, MEL-COR Computer Code Manuals Vol. 2: Reference Manual Version 2.1.6840 2015, Albuquerque (USA), 2015.

[29] J. Tills, A. Notafrancesco, J. Phillips, Application of the MELCOR Code to Design Basis PWR Large Dry Containment Analysis, 2009.

[30] A. Kontautas, The Numerical Study of Aerosol and Radionuclide Transport in the Containments of Nuclear Power Plants, Kaunas University of Technology/ Lithuanian Energy Institute, 2013.

[31] P. Chatelard, S. Arndt, B. Atanasova, G. Bandini, A. Bleyer, T. Brähler, M. Buck, I. Kljenak, B. Kujal, Overview of the independent ASTEC V2.0 validation by SARNET partners, Nucl. Eng. Des. 272 (2014) 136−151.

[32] B. Gonfiotti, S. Paci, Analysis of the THAI Iod-11 and Iod-12 tests: advancements and limitations of ASTEC V2.0R3p1 and MELCOR V2.1.4803, Ann. Nucl. Energy 77 (2015) 451−476.

[33] D.S. Yoon, H.J. Jo, M.L. Corradini, Assessment of MELCOR condensation models with the presence of noncondensable gas in natural convection flow regime, Nucl. Eng. Des. 317 (2017) 110−117.

[34] S. Dickinson, A. Auvinen, Y. Ammar, L. Bosland, B. Clément, F. Funke, G. Glowa, T. Kärkelä, D.A. Powers, S. Tietze, G. Weber, S. Zhang, Experimental and modelling studies of iodine oxide formation and aerosol behaviour relevant to nuclear reactor accidents, Ann. Nucl. Energy 74 (2014) 200−207.

[35] W.C. Hinds, Aerosol Technology: Properties, Behavior, and Measurement of Airborne Particles, 2012.